ACS APPLIED ENERGY MATERIALS

www.acsaem.org

Article

Stability and Hole-Conductivity Advantages of a Spiro[1,3-dithiolane-2,9′-fluorene] Core Relative to a Dibenzothiophene in Hole-Transporting Materials with Outdoor and Indoor Photovoltaic Applications

Nagharsh Mirakyan, Adnan Ahmed, Asta Dabuliene, Edwin Pineda, Ranush Durgaryan, Dmytro Volyniuk, Oleksandr Bezvikonnyi, Graeme Cooke, Lethy Krishnan Jagadamma,* and Juozas Vidas Grazulevicius*

Cite This: https://doi.org/10.1021/acsaem.6c01031

Read Online

ACCESS | Metrics & More | Article Recommendations | Supporting Information

ABSTRACT: Two hole-transporting compounds with the same side-donor moiety and different central fragments, i.e., those of dibenzothiophene or spiro[1,3-dithiolane-2,9′-fluorene] are reported. They are synthesized using microwave irradiation-assisted Buchwald–Hartwig cross-coupling reactions, which are completed within 15–40 min. The solid films of the compounds are characterized by low ionization energies of ca. 5.0 eV. According to charge extraction by linearly increasing voltage (CELIV) and time-of-flight experiments, the spiro[1,3-dithiolane-2,9′-fluorene] derivative exhibits higher hole mobility (1.8×10^{-4} $cm^2/V{\cdot}s$ at an electric field of 3.17×10^5 V/cm) than the dibenzothiophene-based counterpart (4.6×10^{-5} $cm^2/V{\cdot}s$ at the same electric field). Both the compounds are characterized by high electrochemical stability, as evidenced by reversible cyclic voltammograms. The compounds exhibit high glass transition temperatures of 142 and 163 °C, suggesting high morphological stability of their solid amorphous films. The spiro[1,3-dithiolane-2,9′-fluorene] derivative exhibits significantly higher photochemical stability in comparison to that of the dibenzothiophene-based compound, as evidenced by the constant intensity of fluorescence of the toluene solutions and films under UV irradiation. Its films exhibit high conductivity, confirmed by CELIV in the dark. Perovskite solar cells demonstrate the highest stability and efficiency when the spiro[1,3-dithiolane-2,9′-fluorene] derivative is used for the deposition of hole-transporting layers. Under solar and indoor illumination, maximum power conversion efficiencies of 15.5 and 30%, respectively, are achieved, demonstrating the potential of spiro[1,3-dithiolane-2,9′-fluorene] derivatives over dibenzothiophene derivatives in molecular structure designs.

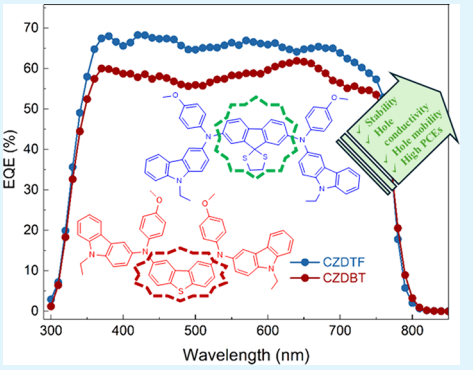

KEYWORDS: *microwave irradiation-assisted Buchwald–Hartwig cross-coupling reaction, dibenzothiophene, spiro[1,3-dithiolane-2-9′-fluorene], indoor and outdoor perovskite solar cells*

INTRODUCTION

Stable and efficient hole-transporting materials (HTMs) obtained via fast, simple, and cost-effective synthetic procedures can bring perovskite solar cells (PSCs) closer to wide commercialization.[1−3] In the molecular design of such HTMs, a range of properties have to be taken into account including trap-free hole transport with high hole mobility; high conductivity; low ionization energy, satisfying efficient hole-extraction capacities; high glass transition temperature and hydrophilicity; optical transparency, allowing solar illumination to reach the light-absorbing layer; and stability of the hole-transporting layer (HTL) and interface, preventing non-radiative recombination in bulk and at interfaces.[4−9] The most widely used HTMs, such as 2,2′,7,7′-tetrakis[*N*,*N*-bis(*p*-methoxyphenyl)amino]-9,9′-spirobifluorene (spiro-OMeTAD), do not satisfy many of the above-listed requirements[10] and require costly and tedious synthetic and purification procedures to realize efficient hole extraction properties.[11−14] Furthermore, the low glass transition temperature of pristine spiro-OMeTAD (~80 °C) often results in the inferior morphological stability of the solid amorphous layer and hence poor solar cell performance.[15] Thus, the perovskite photovoltaic research field urgently demands easy-to-synthesize and low-cost substitutes for spiro-OMeTAD. At the same time, the synthesis and purification of spiro-OMeTAD are complicated and high-priced.[16] The corresponding HTMs

Received: March 26, 2026
Revised: June 25, 2026
Accepted: June 26, 2026

require utilization of dopants, leading to the sophisticated procedure of device fabrication and *J*–*V* hysteresis.[13,14,16–21] Solar cell performance is also negatively affected by the transition of spiro-OMeTAD from an amorphous to a crystalline state at temperatures higher than 120 °C due to the symmetry of spirobifluorene.[16]

Highly efficient PSCs with long-term stability and solar and/or indoor light power conversion efficiencies (PCEs) are developed by depositing dopant-containing HTMs and synthesized via costly multistep routes.[22–25] Due to the constraints of HTMs, highly efficient PSCs generally require doping of HTLs to improve hole mobility and conductivity or the application of self-assembled layers for defect passivation and improved charge extraction properties.[26,27] Therefore, a prevailing trend in the research and development of HTMs for PSCs is the search for the compounds with the optimal set of properties.

The molecular design of many HTMs has recently been based on incorporating sulfur into the molecules, due to their high charge mobility and red-shifted absorption.[7,28–34] The derivatives featuring dibenzothiophene and triphenylamine exhibited high hole mobilities exceeding 1×10^{-3} $cm^2/V{\cdot}s$.[35] The derivative containing methyl sulfide groups reached a high PCE of 22.08% and long-lasting device operation of PSCs.[35] This result was explained by the ability of the HTM-containing methyl sulfide group to reduce nonradiative recombination and charge-transport losses at the HTL/perovskite interface of PSC. We also previously developed a sulfur-containing HTM, i.e., derivatives of dibenzothiophene and carbazole, which exhibited non-dispersive hole transport with a low energetic disorder of 0.0782 eV and a high hole mobility of 9.45×10^{-4} $cm^2/V{\cdot}s$, allowing PSCs with PCEs higher than 20%.[36] Despite the extensive development of spiro derivatives and sulfur-containing HTMs for PSCs, limited information is available on HTMs that integrate the advantages of both the molecular design strategies. As the derivatives of carbazole are widely used in optoelectronic devices due to their electron-donating, thermal and charge transport properties, PSCs with carbazole-based isomeric HTMs were reported to show the promising efficiency of up to 18% under solar illumination.[37]

The alternative approach is the replacement of spiro-OMeTAD with new spiro derivatives. One of the spiro strategies links the aromatic rings to a tetrahedral sp^3-hybridized atom.[28] For instance, *N*^{2},*N*^{7}-bis(4-methoxyphenyl)-*N*^{2},*N*^{7}-di(spiro[fluorene-9,9′-xanthen]-2-yl)spiro[fluorene-9,9′-xanthene]-2,7-diamine (X55) showed higher hole mobility and conductivity values of 6.81×10^{-4} $cm^2/V{\cdot}s$ and 8.43×10^{-4} S/cm, respectively, in comparison to spiro-OMeTAD (1.48×10^{-4} $cm^2/V{\cdot}s$ and 1.43×10^{-4} S/cm) estimated under the same conditions.[29] This enhancement was enabled by an 11% higher relative average PCE of 19.4% for X55-based PSCs, compared to the reference spiro-OMeTAD-containing PSCs with an average PCE of 17.4%. The X55-based PSCs displayed superior long-term operational \stability compared to the devices containing spiro-OMeTAD. Jeong et al.[38] reported spiro derivatives with asymmetric phenylnaphthylamine edge units. They achieved a PCE of 24.43% in comparison to 23.95% PCE of control spiro-OMeTAD-based PSC in conventional n–i–p mesoscopic architecture FTO/cTiO_2/mp-TiO_2/$FAPbI_3$/spiro-Naph/Au and almost 90% PCE retention over 2000 h. Han et al.[39] synthesized a spiro derivative of carbazole, by replacing the methoxy group in spiro-OMeTAD by *N*-ethylcarbazole termination. This HTM reached a PCE of 22.01% utilizing the architecture FTO/bl-TiO_2/mp-TiO_2/$Cs_{0.05}FA_{0.95}PbI_3$/HTM/Au. Zhou et al.[40] reported the synthesis of a hole-transporting derivative with a thiomethyl-substituted fluorene arm and a spiro-[fluorene-9,90-xanthene] core (T2). PSC with the structure ITO/SnO_2/$Cs_{0.05}FA_{0.95}PbI_3$/T2/Au solar cells showed PCEs of 26.52 and 26.47% in FW and RV scans, respectively. Liu et al.[41] synthesized a spiro-type HTM via Buchwald–Hartwig cross-coupling reaction, functionalizing spiro compounds with chlorine atoms. The incorporation of chlorine atoms allowed enhanced hole extraction, by decreasing the interfacial defect density and matching the energy level of the highest occupied molecular orbital (HOMO) with the perovskite valence band. Furthermore, a PCE of over 25% was reported for the device with the structure FTO/SnO_2/$Cs_{0.05}FA_{0.95}PbI_3$/spiro-mCl/Au.

Compared to the extensive efforts on novel HTLs being developed for outdoor perovskite solar cells, very few reports are available which explicitly focus on the hole transport functionality under indoor lighting conditions.[16] Most of the halide perovskite indoor photovoltaic devices still use HTLs inherited and optimized for outdoor (1 sun illumination) perovskite solar cells.[14,42] Since under the low-intensity indoor light conditions, the density of photogenerated carriers is low; to maximize the efficiency, the charge transport layers (CTLs) should have certain characteristics, which are relaxed under high-intensity 1 sun illumination.[43,44] The CTLs should have better shunt properties, as under indoor lighting, the tolerance to series resistance is relatively higher than under 1 sun. Thus, the CTLs should have better charge selectivity and blocking properties to minority carriers. The tolerance to series resistance allows thicker CTLs with suitable energy alignment but less tolerance to leakage paths (high shunt requirement). Additionally, recent efforts on HTL development for indoor photovoltaics have extensively explored self-assembled monolayers (SAMs), which have demonstrated notable advantages, including excellent operational stability and high photovoltaic performance under low-light conditions (PCEs of 40–42%).[45] Nevertheless, SAM-based approaches may also present certain challenges, such as their ultrathin nature providing limited physical buffering against electrode diffusion or surface defects, relatively narrow processing windows, and high surface sensitivity that can increase the susceptibility of buried interfaces to defects and recombination. Furthermore, the presence of acidic anchoring groups has been reported in some cases to impact long-term device stability.[46,47] Given the growing importance of halide perovskite indoor photovoltaics for sustainably powering Internet-of-Things (IoT) technologies within smart-building environments, there is a pressing need to develop new HTMs specifically tailored for halide-perovskite indoor PV applications.[48]

In this study, we explored the benefits and drawbacks of molecular design strategies based on the spiro and sulfur linkages by developing two HTMs, one with a spiro linkage (CZDTF) and one without it (CZDBT). Two compounds featuring the same electron-donating arms but different central cores, i.e., with dibenzothiophene or spiro[1,3-dithiolane-2,9′-fluorene] moieties were designed and synthesized. The spiro[1,3-dithiolane-2,9′-fluorene] derivative demonstrated higher stability, conductivity, hole mobility, and better performance in solar and indoor PSCs than the dibenzothiophene derivative. No dopants were introduced into the HTMs to isolate their intrinsic structural and electronic properties in governing hole extraction and transport. As a consequence, the

https://doi.org/10.1021/acsaem.6c01031
ACS Appl. Energy Mater. XXXX, XXX, XXX–XXX

photovoltaic device performance is not expected to reach that of the optimized devices, with doped HTM systems such as spiro-OMeTAD. Nevertheless, the obtained photovoltaic performance (PCEs of 11–15% under 1 sun and 22–30% under indoor illumination) provides a meaningful basis for comparative analysis between the materials. Our findings suggest that a combination of the spiro approach and the incorporation of sulfur atoms should be used in the molecular design of HTMs to further advance their performance in PSCs.

■ EXPERIMENTAL SECTION

The synthesis of the target compound is presented below. Detailed information regarding the materials utilized and the synthesis of the starting compounds is provided in the Supporting Information.

2′,8′-Bis[(4-methoxyphenyl)(9-ethylcarbazol-3-yl)amino]dibenzothiophene (CZDBT)

A mixture of 2-bromodibenzothiophene (0.40 g, 0.14 mmol), *p*-anisidine (0.19 g, 1.54 mmol), sodium *tert*-butoxide (0.948 g, 9.8 mmol), $Pd_2(dba)_3$ (0.09 g, 0.098 mmol), and XPhos (0.103 g, 0.14 mmol) was added to dry toluene (10 mL). The reaction was performed in a microwave under an argon atmosphere at 130 °C for 30 min. Then, 2,8-dibromodibenzothiophene (0.24 g, 0.7 mmol) was directly added to the reaction mixture. The reaction was performed under the same conditions for 30 min. The target product was purified by column chromatography on silica gel using hexane and ethyl acetate as an eluent mixture of solvents in a volume ratio of 15:1. The yield of yellow powder was 56% (0.320 g).

^{1}H NMR (400 MHz, THF-d_8) δ 7.90 (d, J = 7.7 Hz, 2H), 7.81 (s, 2H), 7,70 (s, 2H), 7.63 (d, J = 8.6 Hz, 2H), 7.42–7.33 (m, 6H), 7.18 (d, J = 8.5 Hz, 2H), 7.10–7.03 (m, 4H), 6.98 (d, J = 8.4 Hz, 4H), 6.73 (d, J = 8.4 Hz, 4H), 4.36 (q, J = 7.0 Hz, 4H), 3.68 (s, 6H), 137 (t, J = 6.8 Hz, 6H). ^{13}C NMR (101 MHz, THF-d_8) δ 156.32, 147.86, 143.33, 141.57, 141.50, 137.69, 137.60, 133.85, 126.38, 125.70, 125.01, 124.16, 124.02, 121.25, 119.27, 117.90, 116.13, 115.27, 110.09, 109.32, 55.53, 38.08, 14.14.

ESI-MS (m/z): calcd for $C_{54}H_{44}N_4O_2S$ $[M]^+$ = 812.3184, found $[M + H]^+$ = 813.2609.

2′,7′-Bis[(4-methoxyphenyl)(9-ethylcarbazol-3-yl)amino]-spiro[1,3-dithiolane-2,9′-fluorene] (CZDTF)

A mixture of 2-bromodibenzothiophene (0.4 g, 1.4 mmol), *p*-anisidine (0.189 g, 1.53 mmol), sodium *tert*-butoxide (0.948 g, 9.8 mmol), $Pd_2(dba)_3$ (0.09 g, 0.098 mmol), and XPhos (0.103 g, 0.14 mmol) was added to dry toluene (7 mL). The reaction was performed in a microwave under an argon atmosphere at 130 °C for 30 min. Then, 2′,7′-dibromospiro[1,3-dithiolane-2,9′-fluorene] (0.29 g, 0.7 mmol) was directly added to the reaction mixture. The reaction was performed under the same conditions for 30 min. The target product was purified by column chromatography on silica gel using hexane and ethyl acetate as an eluent mixture of solvents in a volume ratio of 6:1. The yield of yellow powder was 24% (0.150 g).

^{1}H NMR (400 MHz, THF-d_8) δ 7.95 (d, J = 7.7 Hz, 2H), 7.89 (s, 2H), 7.44–7.24 (m, 12H), 7.08 (d, J = 6.3 Hz, 6H), 6.82 (d, J = 7.9 Hz, 6H), 4.40 (d, J = 6.2 Hz, 4H), 3.74 (s, 6H), 3.40 (s, 4H), 1.40 (t, J = 6.6 Hz, 6H). ^{13}C NMR (101 MHz, THF-d_8) δ 156.46, 152.24, 149.07, 143.01, 141.31, 141.30, 137.72, 126.38, 126.19, 123.58, 121.07, 119.74, 119.15, 118.45, 115.10, 115.04, 109.89, 109.14, 69.44, 53.33, 42.26, 37.91, 13.95.

ESI-MS (m/z): $C_{57}H_{48}N_4O_2S_2$ $[M]^+$ = 884.3219, found $[M]^+$ = 885.2698.

Instrumentations and characterization methods of HTMs are detailed in the Supporting Information. Additionally, the Supporting Information outlines the methodology for fabricating and testing PSCs.

■ RESULTS AND DISCUSSION

Synthesis

The disubstituted dibenzothiophene and spiro[1,3-dithiolane-2,9′-fluorene] derivatives were synthesized, as shown in Scheme 1. The microwave-assisted Buchwald–Hartwig cross-coupling reactions of *p*-anisidine with the respective bromo compounds afforded the corresponding intermediates. The further Buchwald–Hartwig cross-coupling reactions with the corresponding intermediate dibromo compounds gave the target derivatives (Scheme 1). The products were purified by column chromatography. The newly synthesized compounds were identified by mass spectrometry, ^{1}H, ^{13}C NMR spectroscopy

Scheme 1. Synthesis of Compounds CZDBT and CZDTF: (i) *t*-BuONa, $Pd_2(dba)_3$, X-Phos, Toluene, 130 °C, Microwave Irradiation, 15–40 min

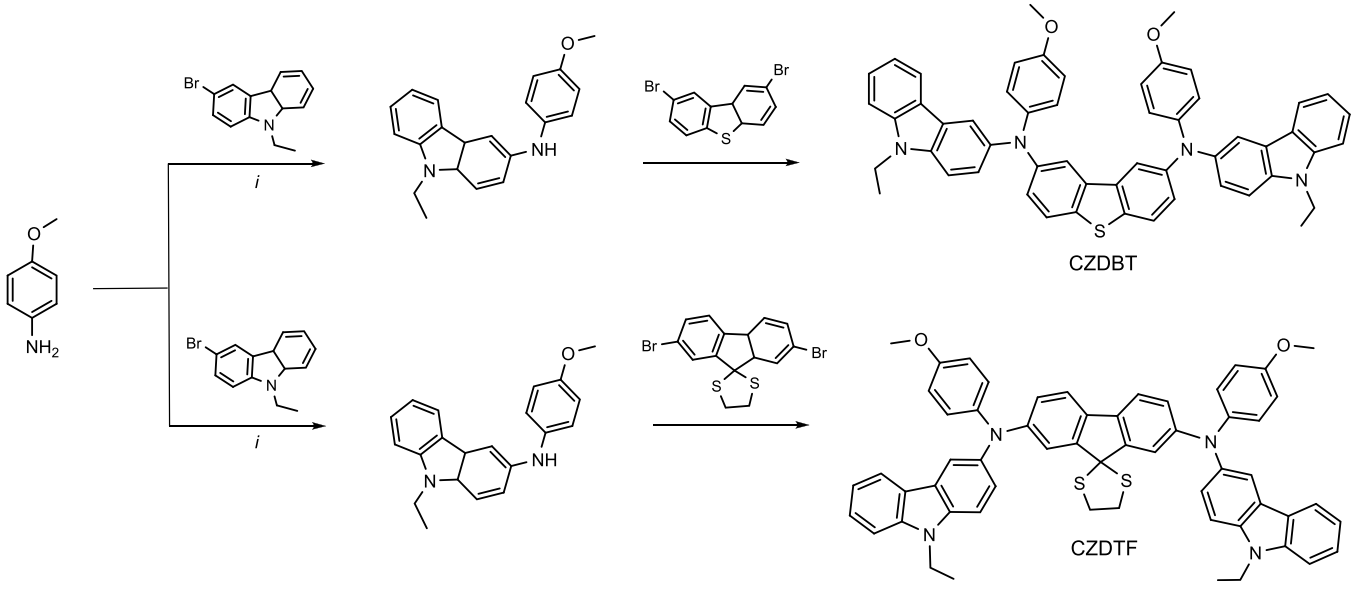

https://doi.org/10.1021/acsaem.6c01031
ACS Appl. Energy Mater. XXXX, XXX, XXX–XXX

(Figures S1–S4). The data were found to be in good agreement with the proposed structures.

Thermal Transitions

Both synthesized compounds were found to be fully amorphous. The information on the morphology of the films of the compounds was derived using a non-contact, white-light interferometry profilometer. The line skewness and kurtosis, estimated according to the ASME B46.1 2D standard, were found to be –0.16 and 2.8 for CZDBT and –0.04 and 3.1 for CZDTF, respectively. The obtained results prove the amorphous nature of the layers characterized by symmetrical, Gaussian randomness with no distinct facets. The thermal investigation of the compounds was carried out by differential scanning calorimetry (DSC) and thermogravimetric analysis (TGA) under a nitrogen atmosphere. The results are presented in Table 1. The signals of only glass transitions were observed in the heating and cooling DSC scans (Figure 1a). Peaks due to crystallization or melting did not appear in cooling and heating cycles between 10 and 200 °C (Figure S5). The glass transition temperatures (T_g) obtained from the repeated heating scans were found to be of 142 and 163 °C for compounds CZDBT and CZDTF, respectively (Figures 1a and S5). The TGA data show that the thermal stability of the dibenzothiophene derivative is higher than that of

Table 1. Thermal, Optical, Electrochemical, and Photoelectrical Characteristics of Compounds CZDBT and CZDTF

	$T_{-5\%}$, °C[a]	T_g,[b] °C	IE_{CV}, eV[c]	λ_{abs}, nm[d]	λ_{PL}, nm[d]	IE_{PE}, eV[e]	E_g^{opt}, eV[f]	EA_{PE}, eV[g]	μ_h, $cm^2/V{\cdot}s$[h]
CZDBT	408	142	4.81	393[i]	448	5.04	2.63	2.41	4.8×10^{-5}
CZDTF	314	163	4.69	383	437	5.03	2.8	2.23	1.7×10^{-4}

[a]$T_{-5\%}$—5% mass loss temperature determined by TGA, heating rate 20 °C/min, N_2 atmosphere. [b]T_g—glass transition temperature, determined by DSC, scan rate 10 °C/min, N_2 atmosphere: second heating scan. [c]$IE_{CV} = -(E_{onset(ox1)}) + 4.8$). [d]Wavelengths of low-energy band absorption peaks (λ_{abs}) and wavelengths of the maxima of photoluminescence spectra of toluene solutions. [e]Ionization energy (IE_{PE}) measured by PE spectrometry. [f]E_g^{opt} is the optical bandgap (Figure S7). [g]Electron affinities (EA_{PE}) determined by the equation $EA_{PE} = IE_{PE} - E_g^{opt}$. [h]At an electric field of 3.2×10^5 V/cm. [i]Shoulder.

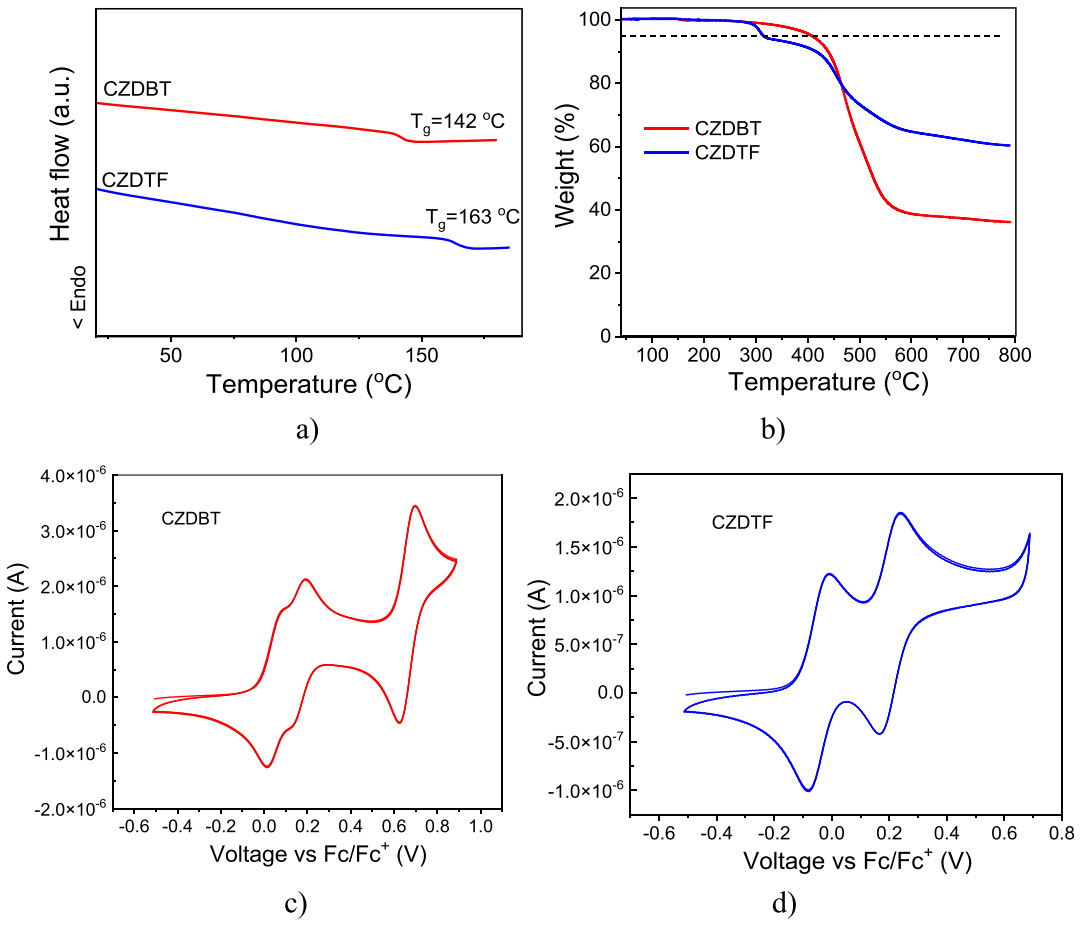

Figure 1. DSC thermograms of second heating scans recorded at a heating rate of 10 °C/min in a nitrogen atmosphere (a), TGA curves recorded at a heating rate of 20 °C/min in a nitrogen atmosphere (b) of compounds CZDBT and CZDTF. Cyclic voltammograms of compounds CZDBT (c) and CZDTF (d) recorded for 0.1 M Bu_4NBF_4/dichloromethane solutions at a scan rate of 0.1 mV/s.

https://doi.org/10.1021/acsaem.6c01031
ACS Appl. Energy Mater. XXXX, XXX, XXX–XXX

the spiro[1,3-dithiolane-2,9′-fluorene]-based compound. For the synthesized spiro[1,3-dithiolane-2,9′-fluorene]-based compound, thermal degradation was observed in two stages (Figure 1b). The dibenzothiophene derivative CZDBT demonstrated 5% weight loss at a temperature of 408 °C, whereas the compound CZDTF exhibited 5% weight loss at a temperature of 314 °C.

Electrochemical Properties

The electrochemical properties of the dibenzothiophene and spiro[1,3-dithiolane-2,9′-fluorene] derivatives (CZDBT and CZDTF) were studied by cyclic voltammetry (CV). Electrochemical data collected are given in Table 1. The cyclic voltammograms of the solutions of the compounds in dichloromethane (DCM) were recorded using tetrabutylammonium hexafluorophosphate ($TBAHFP_6$) as the electrolyte (Figure 1c,d). CZDBT exhibited three quasi-reversible oxidation peaks and reduction peaks in the range of −0.10 to 0.70 V. CZDTF showed two oxidation peaks and reduction peaks in the same range. It should be noted that observation of the reversible cyclic voltammograms indicates high electrochemical stability of compounds.[49] The values of ionization energies (IE_{CV}) estimated from the onsets of oxidation potentials are collected in Table 1.

Theoretical Studies

We have modeled CZDBT and CZDTF using density functional theory using the ωB97XD functional and the 6-31G(d,p) basis set. The HOMO and LUMO maps are shown in Figure 2. For CZDBT, the HOMO is localized over the central core and one of the side-arm residues, whereas the LUMO extends over the core and the appendages. For CZDTF, the HOMO extends across the core and appendages, whereas the LUMO is more localized over one of the appendages. The calculated LUMO energies of both derivatives are identical (0.9 eV), whereas the calculated HOMOs show a larger variation −5.97 eV (CZDTF) versus −6.20 eV (CZDBT), presumably resulting from the different donor abilities of the core moieties (Table 2). Likewise, the calculated dipole moments differ significantly for the two derivatives, with CZDBT having a dipole moment of 3.31 D, whereas CZDTF has a dipole moment of 5.15 D (Table 2), reflecting the polarity and geometry differences of the core units of the two derivatives.

Photophysical Properties

Low-energy bands within the wavelength range of ca 350–430 nm were observed in the absorption spectra of dilute toluene and THF solutions, as well as of the neat films of compounds CZDBT and CZDTF (Figure 3a,b). These bands can be attributed to intramolecular charge transfer from the side-located aromatic amino moieties to the central dibenzothiophene (in case of CZDBT) or spiro[1,3-dithiolane-2,9′-fluorene] (in case of CZDTF) fragments. In the spectra of the compound CZDTF, low-energy absorption bands were recorded. Their peaks were observed at 383 nm for the solution in toluene, at 380 nm for the solution in THF, and at 390 nm for the film. It appears that more intensive charge transfer is characteristic of the compound CZDTF in comparison to that of the compound CZDBT. This statement aligns with the trend of molar absorption coefficients (ε) of toluene solutions of CZDBT and CZDTF measured at various wavelengths. For example, the solution of CZDTF is characterized by ε of 2.6 × 10^3 M^{-1} cm^{-1} at 380 nm, which is higher than that of the solution of CZDBT (0.95 × 10^3 M^{-1} cm^{-1}) recorded at the same wavelength. A similar trend was observed for the absorption coefficients of the films of CZDBT and CZDTF at around 395 nm. Figure 3e displays the ultraviolet–visible absorption spectra of thin films of CZDBT and CZDTF. Both the films exhibit absorption peaks at around 395 nm. In addition, CZDTF shows strong absorbance, close to 385 nm reported for spiro-OMeTAD.[50] The differences in the energies of absorption maxima of the low-energy bands of the films of CZDBT and CZDTF can be attributed either to the polarity effects or to intermolecular interactions in the solid state.

The photochemical stability of CZDBT and CZDTF was tested under continuous UV illumination of the toluene solutions and films (Figures 3c,d and S6). Their toluene solutions and films emit blue light under ultraviolet (UV) excitation at 350 nm. The photoluminescence (PL) spectra peak at 448 and 460 nm for CZDBT and at 437 and 440 nm for CZDTF. To exclude the effect of the transformation of oxygen triplet into singlet states under UV excitation on PL intensity, the spectra of deoxygenated toluene solutions of CZDBT and CZDTF by a flow of inert gas were investigated (Figure S6). PL intensity of the toluene solution of CZDTF remained stable after 10 cycles of recording of PL spectra. In contrast, the intensity of the emission band of the toluene solution of CZDBT decreased to 86% of its original intensity. After 15 cycles of recording of PL spectra, the initial PL intensity (I_0) of the films of CZDBT and CZDTF decreased to 0.3 × I_0 and 0.8 × I_0, respectively (Figure 3c,d). It is evident that the derivative of spiro[1,3-dithiolane-2,9′-fluorene] (CZDTF) exhibits higher photochemical stability compared to the derivative of dibenzothiophene (CZDBT). The photochemical stability of HTMS can have an effect on the stability of PSCs.

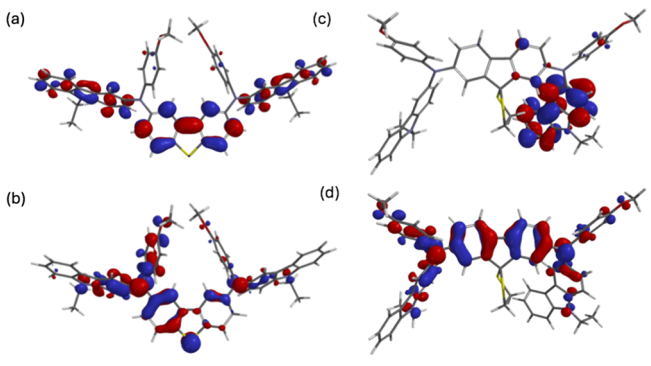

Figure 2. The computed LUMO (a) and HOMO (b) maps of CZDBT and LUMO (c) and HOMO (d) maps of CZDTF.

Table 2. Showing the HOMO, LUMO Energies, and Dipole Moments for Compounds CZDBT and CZDTF

compound	HOMO, eV	LUMO, eV	dipole moment, D
CZDBT	−6.20	0.90	3.31
CZDTF	−5.97	0.90	5.15

Photoelectron Emission Spectroscopy Data

The energy barrier-free extraction of holes at the interface between the anode and HTLs is necessary for efficient PSCs.[51,52] Ionization energies (IE_{PE}) of vacuum-deposited layers of CZDBT and CZDTF were measured by photoelectron emission (PE) spectroscopy in air, with a setup similar to that

https://doi.org/10.1021/acsaem.6c01031
ACS Appl. Energy Mater. XXXX, XXX, XXX−XXX

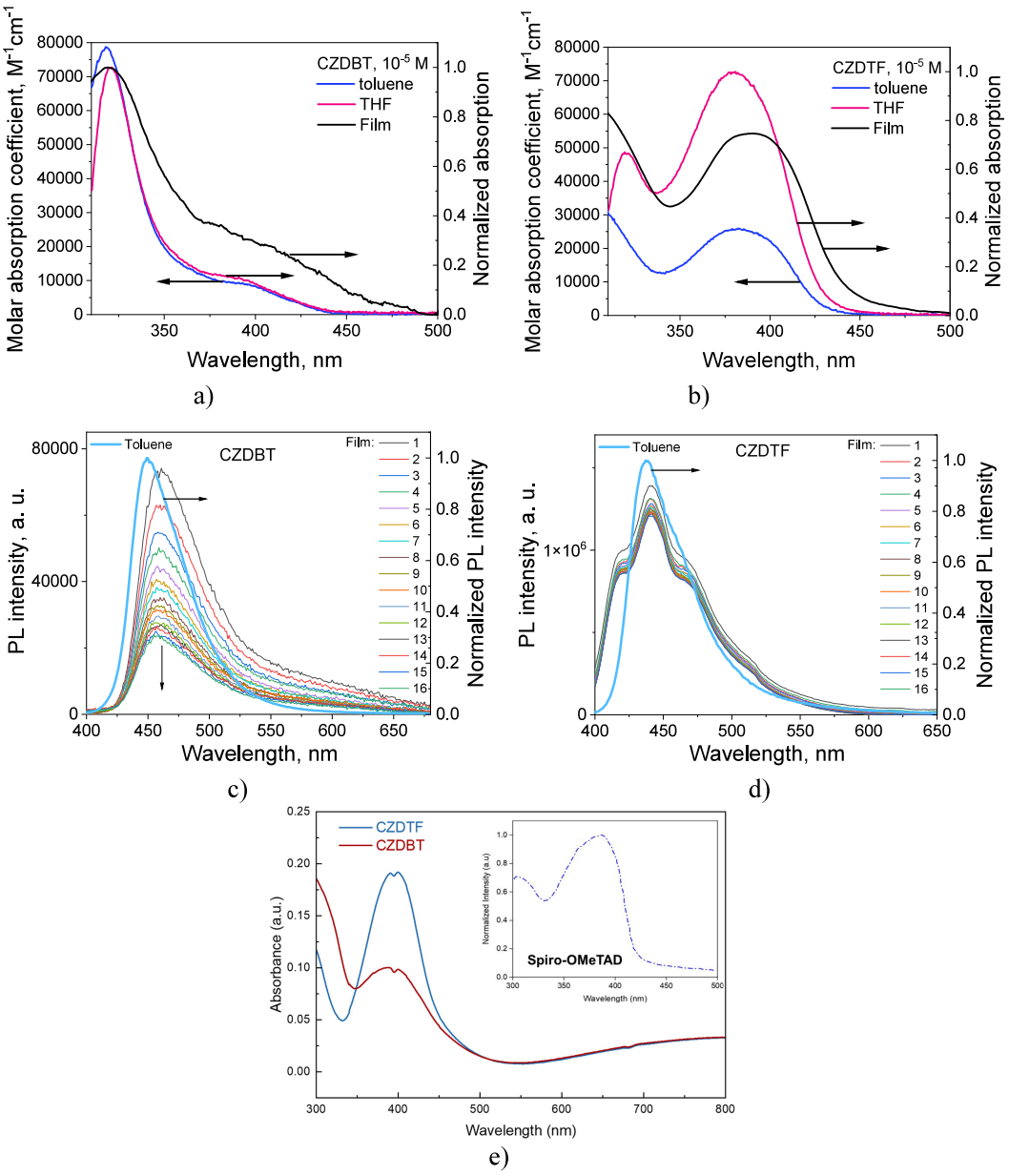

Figure 3. Absorption (a, b) and PL (c, d) spectra of toluene or THF solutions and films of CZDBT and CZDTF. PL spectra of the films were scanned under continuous UV excitation for 30 min. Ultraviolet–visible absorption spectra (e) of thin films of CZDBT and CZDTF and spiro-OMeTAD (inset).

described elsewhere.[53] CZDBT and CZDTF showed low IE_{PE} values of ca. 5 eV (Figure 4a). This value is almost identical to the ionization energy of spiro-OMeTAD (4.94 eV), suggesting similar charge-extraction properties.[30] Absorption spectra of the films of compounds CZDBT and CZDTF were used to obtain the optical band gap energy (E_g^{opt}) (Figure S7). Subtracting E_g^{opt} from the IE_{PE}, the electron affinities (EA_{PE}) of 2.41 and 2.23 eV were obtained for compounds CZDBT and CZDTF, respectively (Table 1). The indirectly measured EA_{PE} values indicate that compounds CZDBT and CZDTF can prevent the loss of mobile electrons by extracting them from the perovskite light-absorbing layer into HTLs of the derivatives of dibenzothiophene or spiro[1,3-dithiolane-2,9′-fluorene].

Charge-Transporting Properties

For the investigation of the charge-transporting properties of the vacuum-deposited layers of CZDBT and CZDTF with the thicknesses (d) exceeding one micrometer (Figure S8), current transients of the samples with the structure glass/indium tin oxide (ITO)/organic layer/Al were recorded by applying the technique of charge carrier extraction by linearly increasing voltage (CELIV).[54,55] In the dark, when the organic layers do not contain photogenerated charges, dark-CELIV signals result from the extraction of equilibrium carriers.[56] Typically, dark-CELIV signals with rectangular shapes are observed for the layers of most organic semiconductors because of the very low concentration of mobile charge carriers in such layers.[57,58]

https://doi.org/10.1021/acsaem.6c01031
ACS Appl. Energy Mater. XXXX, XXX, XXX–XXX

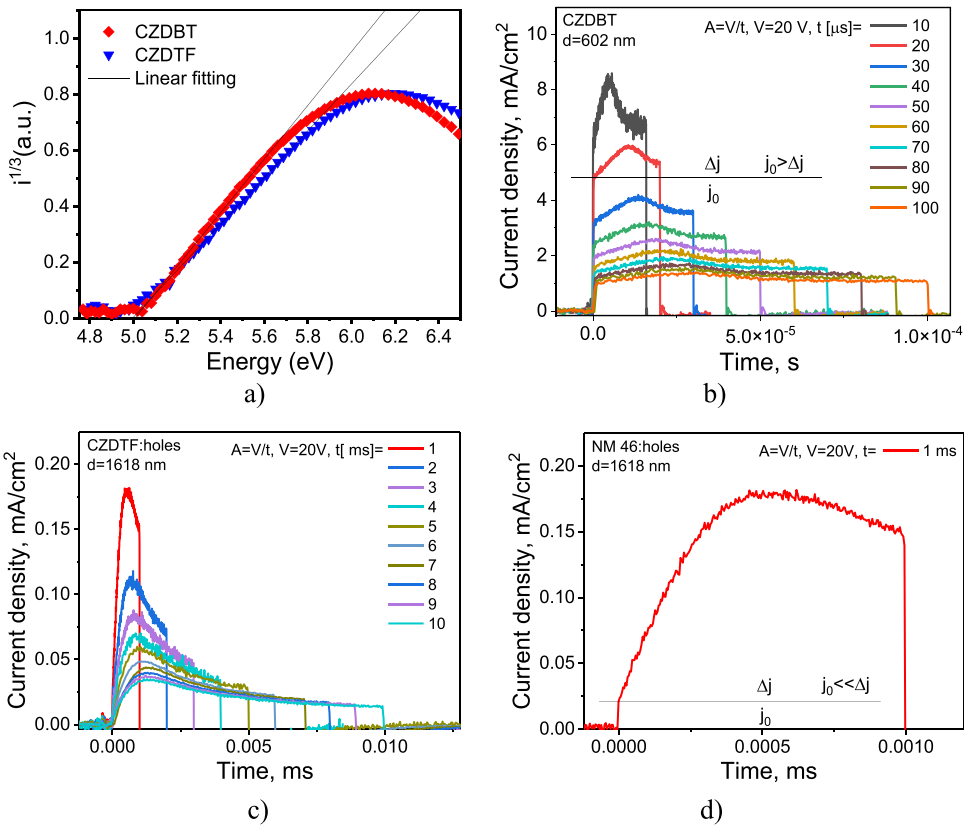

Figure 4. Photoelectron emission spectra of vacuum-deposited films (a) and CELIV signals (b–d) of the samples of CZDBT or CZDTF observed at different durations (t) of triangle pulses and constant voltage of 20 V.

Such dark-CELIV signals include the current density component j_0, arising only from the capacitance response of the ITO/organic layer/Al capacitor, which is charged by the displacement current. Therefore, to study the charge-transporting properties of the organic layers in the dark-CELIV regime, bias voltages are usually applied.[59] However, the mobile carriers in the layers of CZDBT and CZDTF were detected by dark-CELIV measurements without bias voltages (Figure 4b–d). This observation indicates the presence of mobile equilibrium carriers in these layers.

The recorded CELIV current transient curves ($j(t)$) contained the current density component j_0 caused by the capacity response and the extracted current density component (Δj) caused by the extraction of mobile carriers from the layers of CZDBT and CZDTF. The following formula 1 can describe the dark-CELIV signals.[60]

$$j(t) = j_0 + \Delta j(t) = \varepsilon\varepsilon_0 \frac{dE(x,t)}{dt} + \sigma(x,t)E(x,t) \qquad (1)$$

where ε and ε_0 are the dielectric permittivity of the layers and vacuum permittivity, respectively, E is the electric field, and σ is the bulk conductivity of layers containing equilibrium free carrier charges with a certain concentration n_0. The conductivity can be expressed by the equation $\sigma = e\mu n_0$, where e is the elementary charge and μ is the charge carrier mobility. It should be noted that holes are the dominant mobile carriers in the layers of CZDBT and CZDTF, as it is determined by the time-of-flight (TOF) experiment (Figure 5). The observed current density component Δj allows us to calculate hole mobility values at different electric fields and to discuss the hole conductivity of CZDBT and CZDTF. After the analysis of the shapes of CELIV signals, it can be concluded that CZDBT with $j_0 > \Delta j$ is a low-conductivity material, while CZDTF characterized by $j_0 << \Delta j$ is a highly conductive material.[61]

The layers of CZDTF and CZDBT showed hole mobilities of 1×10^{-5} cm^2/V·s at different electric fields of 2×10^4 and 9.8×10^4 V/cm, respectively. The electric field dependencies of hole mobilities of CZDTF and CZDBT are in very good agreement with the results of TOF measurements (Figure 5). The TOF method has limitations when studying semiconductors with high conductivity, as the concentration of bulk mobile carriers may significantly exceed that of interface-generated mobile carriers. However, it was not the case with CZDBT and CZDTF, at least at low electric fields. The transit times (t_{tr}) obtained from the TOF current transients in log–log scales for vacuum-deposited layers of CZDBT and CZDTF were well observed in the wide range of electric fields. For the calculation of hole mobility values, the t_{tr} values were taken at the intersection of two extrapolated lines that reflect the different slopes of the TOF signals. The calculated hole mobilities are plotted in Figure 5 according to the Poole–Frenkel predictions. At an electric field of 3.2×10^5 V/cm, CZDBT and CZDTF showed hole

https://doi.org/10.1021/acsaem.6c01031
ACS Appl. Energy Mater. XXXX, XXX, XXX–XXX

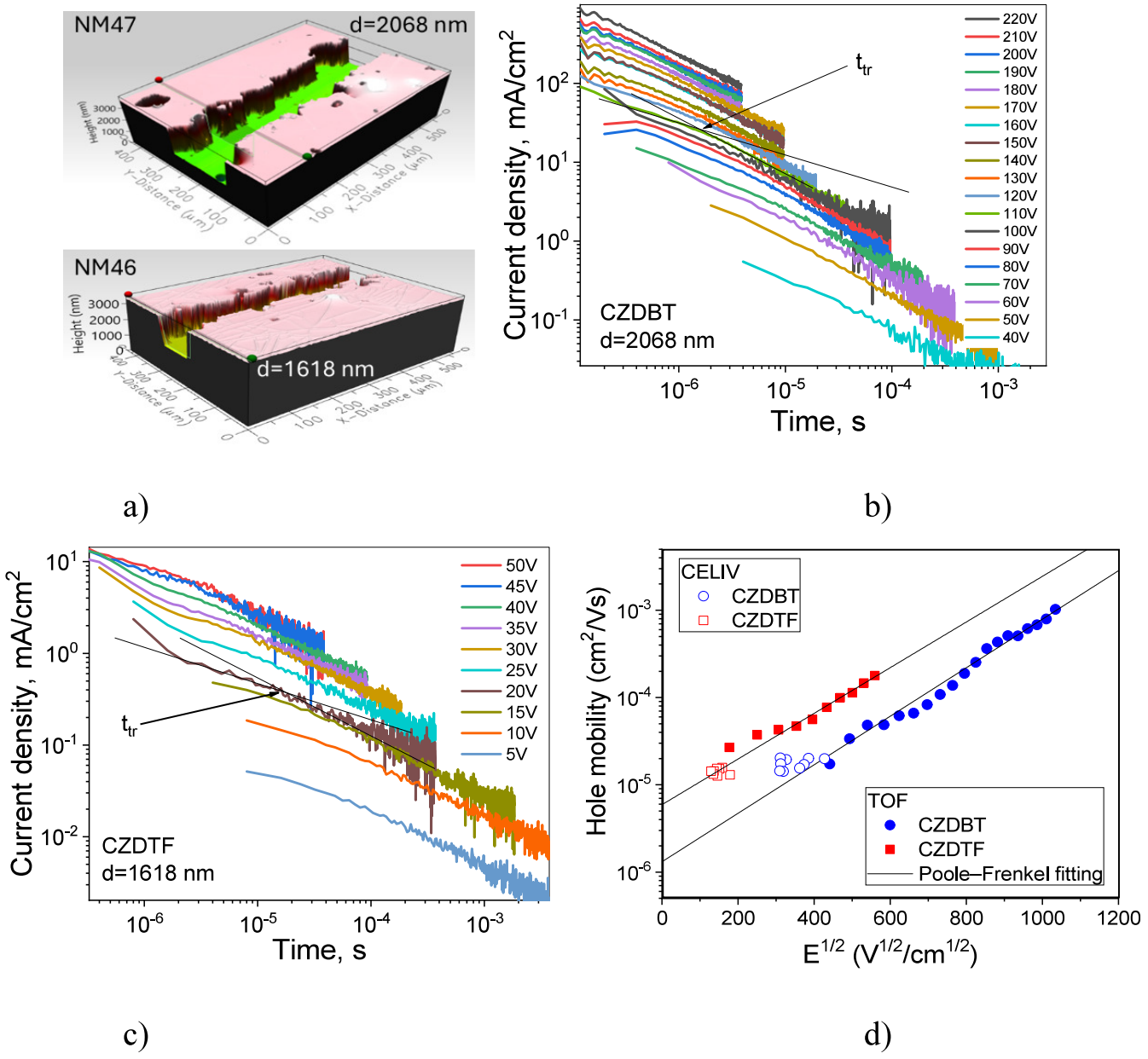

Figure 5. Thickness measurements (a), TOF signals (b, c), and electric field dependencies of hole mobilities for the vacuum-deposited layers (d) of compounds CZDBT and CZDTF.

mobilities of 4.8×10^{-5} and 1.7×10^{-4} $cm^2/V{\cdot}s$, respectively. Because of low conductivity, the TOF current transients were recorded at high electric fields up to 1×10^6 V/cm. At this electric field, CZDBT showed a hole mobility of 1×10^{-3} $cm^2/V{\cdot}s$. Using Poole–Frenkel fitting, hole mobility higher by a factor of three (3×10^{-3} $cm^2/V{\cdot}s$) was expected for CZDTF. Because of the high conductivity of the CZDTF layer, this prediction lacks experimental support. Nonetheless, the CELIV/TOF results suggest higher potential of CZDTF as HTM for PSCs.

Performance in Indoor and Outdoor Perovskite Solar Cells

A set of experimental characterizations suggests that the spiro[1,3-dithiolane-2,9′-fluorene]-containing HTM CZDTF should outperform the dibenzothiophene-based HTM CZDBT in photovoltaic devices, with respect to both stability and efficiency. To support this expectation, three HTMs, CZDBT, CZDTF, and spiro-OMeTAD (serving as refs[10–16]), were further used in a comparative study of their performances in PSCs. We systematically investigated the impact of different processing conditions for CZDTF and CZDTB as HTLs on perovskite solar cells. We fabricated a typical n–i–p perovskite solar cell architecture with the configuration ITO/SnO_2/$MAPbI_3$/HTL/Au. Current density–voltage (*J*–*V*) measurements were performed under 1 sun (AM 1.5 G) and indoor illumination under 1000 lx, 2700 K daylight white LED (with irradiance 0.32 mW/cm^2).

Figure 6 shows the statistical distribution of power conversion efficiency (PCE) and *J*–*V* curves of champion devices with CZDTF and CZDTB as HTLs on perovskite solar cells with $MAPbI_3$ as the active layer. The corresponding performance

https://doi.org/10.1021/acsaem.6c01031
ACS Appl. Energy Mater. XXXX, XXX, XXX–XXX

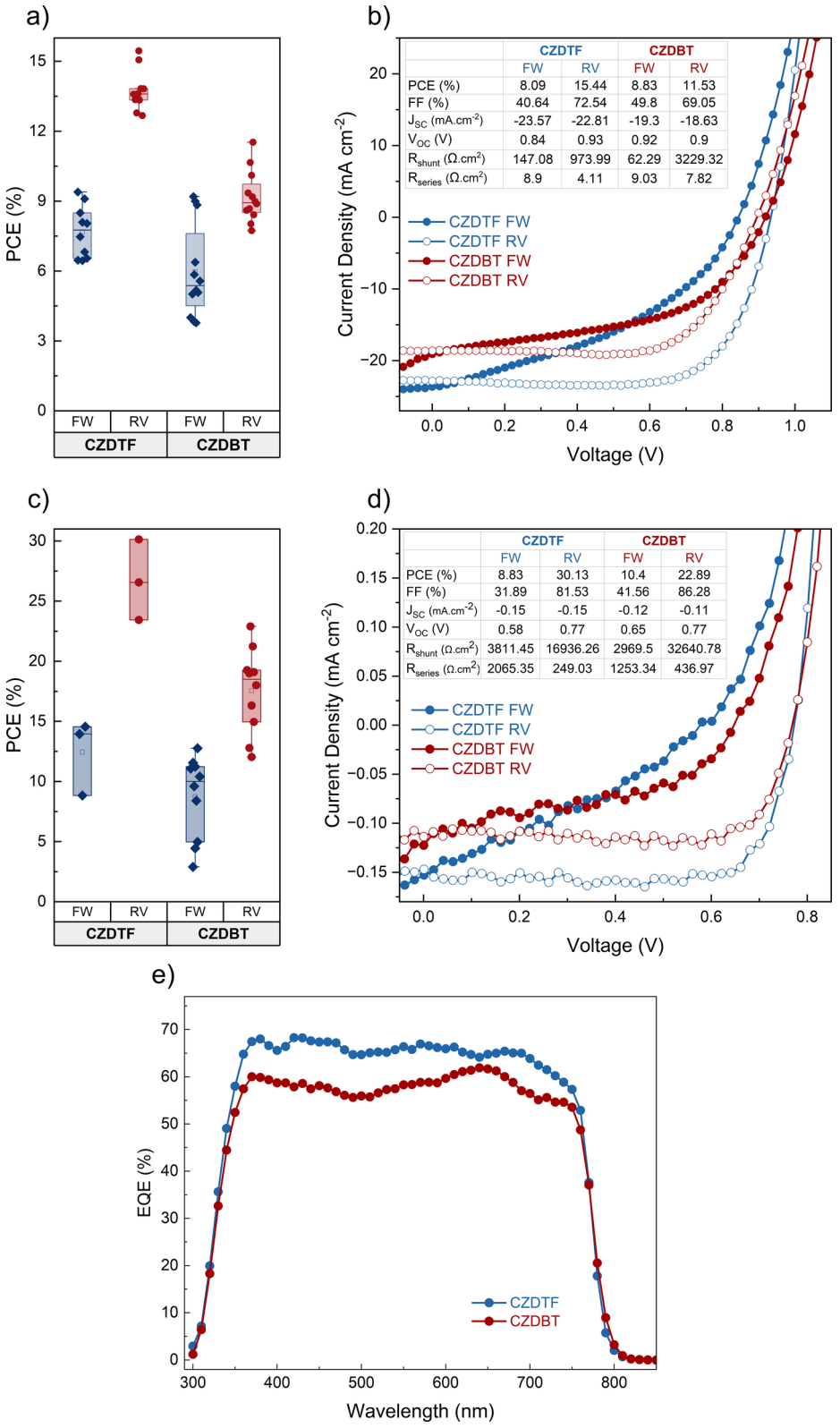

Figure 6. Statistical distribution of PCE values and *J*–*V* curves of champion devices of CZDTF and CZDBT HTMs under 1 sun (a, b) and indoor light illumination (c, d), respectively, and their EQE (e).

parameters are shown in Figure S9. Devices based on CZDTF showed overall champion PCEs of 8.09 and 15.44% with open-circuit voltages (V_{OC}) of 0.84 and 0.93 V, short-circuit current densities (J_{SC}) of 23.57 and 22.81 mA/cm^2, and fill factors (FF) of 40.64 and 72.54% for forward (FW) and reverse (RV) scans, respectively. While devices based on CZDBT

https://doi.org/10.1021/acsaem.6c01031
ACS Appl. Energy Mater. XXXX, XXX, XXX–XXX

showed the best PCE of 8.83 and 11.53% with V_{OC} of 0.92 and 0.90 V, J_{SC} of 19.3 and 18.63 mA/cm^2, and FF of 49.80 and 69.05% for FW and RV scans, respectively. The statistical distribution of PCE and other photovoltaic metrics demonstrates that the PCEs (RV) of CZDTF-based devices are primarily attributed to the increased J_{SC} (Figure S9b), which is in alignment with the lower series resistance of the corresponding devices (Figure S9e). This could be due to the enhanced hole mobility of the CZDTF molecules, as observed from the CELIV measurements. However, the hysteresis index (HI = $PCE_{RV} - PCE_{FW}/PCE_{RV}$) is higher for CZDTF-based devices than for CZDTB, 0.48 and 0.23, respectively. The superior performance of the CZDTF-based photovoltaic devices is further confirmed by external quantum efficiency (EQE) spectra, as illustrated in Figure 6e. To compare the photovoltaic properties of the devices incorporating new HTLs of CZDTF and CZDTB, control devices were fabricated using the layer of spiro-OMeTAD as the HTL. The *J*–*V* characteristics and performance parameters of the corresponding devices under 1 sun are given in Figure S11. The devices based on spiro-OMeTAD HTL showed overall PCEs of 11.9 and 15.8% with open-circuit voltages (V_{OC}) of 1.09 and 1.09 V, short-circuit current densities (J_{SC}) of 21.3 and 21.1 mA/cm^2, and fill factors (FF) of 51.3 and 69.1% for forward (FW) and reverse (RV) scans, respectively. Thus, CZDTF HTL-based devices show a very similar photovoltaic performance to that of the benchmark spiro-OMeTAD HTL. However, it is to be noted that the spiro-OMeTAD HTL in these devices is not pristine but doped with oxygen, TBPi, LiTFSi, and FK-209 to modify their morphological features, energy-level alignment, and transport properties. Meanwhile, the CZDTF and CZDTB HTLs are used in their pristine stage without any further modification or additional dopants.[62]

Under indoor illumination, both HTLs exhibited pronounced scan direction dependence. CZDTF-based devices outperformed the CZDTB ones with outstanding PCEs of 8.83 and 30.13% for FW and RV scans, respectively, whereas CZDTB showed 10.4 and 22.89% for both directions. In terms of FF, CZDTF rose from 31.89% (FW) to 81.53% (RV), while CZDBT increased from 41.56 to 86.28%. The determining factor in the PCE is the higher $J_{SC} \sim 0.15$ mA/cm^2, of the CZDTF-based devices in comparison to $J_{SC} \sim 0.12$ mA/cm^2 produced by CZDTB-based devices. Under indoor illumination, the corresponding devices incorporating spiro-OMeTAD as the HTM showed the highest PCEs of 17 and 31.1% for FW and RV scans, respectively, and are again comparable to the performance of devices incorporating CZDTF as the HTM (Figure S11a,b). The EQE of the spiro-OMeTAD containing devices is also given in Figure S11c. It is to be noted that the indoor PCE shown by the devices incorporating the CZDTB and CZDTF is not world-class leading and show clear *J*–*V* hysteresis. This implies that further optimization of the HTMs may be necessary by incorporating dopants to enhance the hole mobility or the energy-level alignment with the perovskite active layer. The previously reported high PCEs of 40% in perovskite-based indoor PV have been achieved by using the (wide) bandgap-optimized perovskite active layer and the specially optimized transport layers based on perylene diimide (PDI)[63] and advanced interfacial layers using self-assembled monolayers.[45] The indoor PV PCE shown by the devices incorporating CZDTB and CZDTF HTMs is comparable to that of the dopant-free spiro-OMeTAD (~24 to 20%), as previously reported.[62] However, it is worth adding that the *J*–*V* hysteresis of the devices incorporating CZDTB and CZDTF as HTMs is relatively higher than the undoped and doped spiro-OMeTAD HTM-based devices.

As seen in Figure 6, under both outdoor and illumination conditions, devices incorporating CZDTF HTL showed slightly higher photovoltaic performance compared to the devices incorporating CZDTB. This increased performance is mainly due to the higher short-circuit current and low sheet resistance. To identify any correlation between this observation and the morphological features of the HTLs, scanning electron microscopy (SEM) imaging was carried out on the partial device heterostructures (ITO/SnO_2/perovskite active layer/new HTLs). The corresponding SEM images are shown in Figure S12. The morphological features of the HTL of CZDTF comprise an entwined network of interconnected nanowires with a longer aspect ratio, whereas for the HTLs of CZDTB, the morphology is less interconnected with a lower aspect ratio. Thus, the enhanced J_{SC} and lower series resistance of the photovoltaic devices comprising HTL of CZDTF can be attributed to these favourable morphological features for charge collection, which in turn can also be responsible for higher hole mobility, as revealed through the CELIV studies (Figure 5).

Comparing the two HTLs, it is notable that under both illumination conditions, the devices incorporating CZDTF HTLs showed higher *J*–*V* hysteresis compared to CZDTB. In our earlier studies, comparing spiro-OMeTAD and P3HT as HTLs, spiro-OMeTAD based devices showed higher hysteresis compared to P3HT, and this behavior was primarily attributed to the presence of lithium dopants.[14] In the present case, however, neither HTL is doped, and the material under investigation is not spiro-OMeTAD itself but merely shares a similar spiro-linked core. This suggests that the increased hysteresis may not arise from ionic additives, but instead from intrinsic characteristics associated with the spiro-type molecular framework, such as differences in molecular packing, interfacial energetics, or interaction with migrating ionic species at the perovskite/HTL interface. The orthogonal spiro-linkage can disrupt π–π stacking, leading to greater susceptibility to interfacial trap formation, which can contribute to enhanced *J*–*V* hysteresis.[64]

The effect of thermal annealing on the output parameters of PSCs was further investigated (Section S6 and Figures S13–S18, Supporting information). However, this approach did not improve the PCEs.

Finally, we studied the long-term shelf-life stability over more than 120 days of both CZDTF and CZDBT HTL-based devices (which are not encapsulated) and stored in a nitrogen box. As shown in Figure 7, the shelf-life measurements reveal that CZDTF champion devices exhibit good stability during the shelf-life study period. CZDTF retained its PCE over the period of study, with a slight increase from 15.44 to 15.96% for RV scans, mainly due to a small increase in FF from 72.54 to 76.59% and almost constant V_{OC} and J_{SC}. However, in FW scans, there is a drop in PCE from 8.09 to 7.41%, and in FF from 40.64 to 37.41%. For the devices measured after 36 days, the PCE spread was matching that of fresh devices. However, for the devices measured after 121 days, the yield of the working devices was drastically reduced with PCE mostly in the range of 1%. This performance drop is found to be a combined collapse of all the photovoltaic performance parameters, as shown in Figure S19. The performance drop in CZDBT HTL-based devices also showed a similar trend as that of CZDTF

https://doi.org/10.1021/acsaem.6c01031
ACS Appl. Energy Mater. XXXX, XXX, XXX–XXX

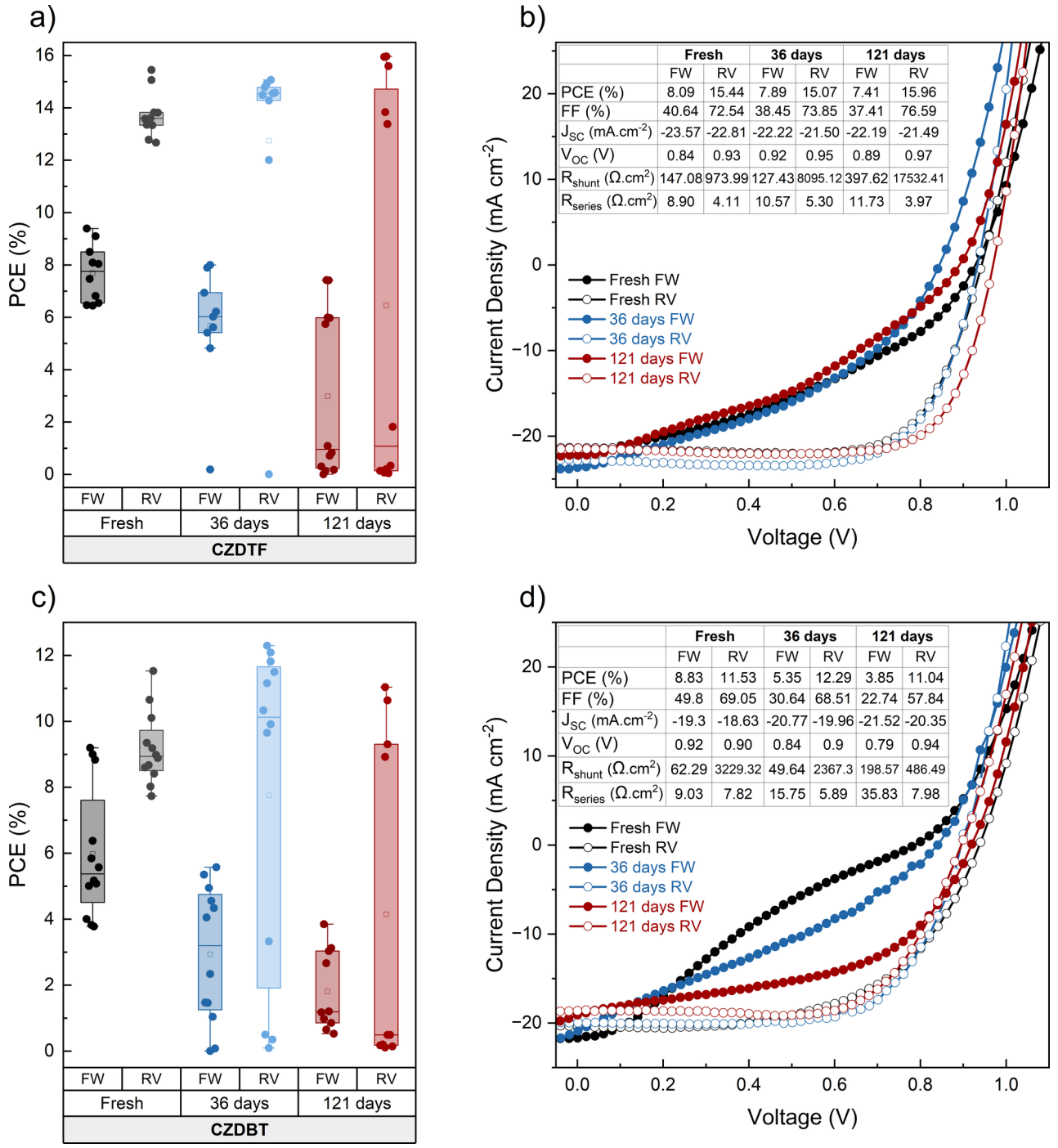

	Fresh		36 days		121 days	
	FW	RV	FW	RV	FW	RV
PCE (%)	8.09	15.44	7.89	15.07	7.41	15.96
FF (%)	40.64	72.54	38.45	73.85	37.41	76.59
J_{SC} (mA.cm^{-2})	-23.57	-22.81	-22.22	-21.50	-22.19	-21.49
V_{OC} (V)	0.84	0.93	0.92	0.95	0.89	0.97
R_{shunt} (Ω.cm^2)	147.08	973.99	127.43	8095.12	397.62	17532.41
R_{series} (Ω.cm^2)	8.90	4.11	10.57	5.30	11.73	3.97

	Fresh		36 days		121 days	
	FW	RV	FW	RV	FW	RV
PCE (%)	8.83	11.53	5.35	12.29	3.85	11.04
FF (%)	49.8	69.05	30.64	68.51	22.74	57.84
J_{SC} (mA.cm^{-2})	-19.3	-18.63	-20.77	-19.96	-21.52	-20.35
V_{OC} (V)	0.92	0.90	0.84	0.9	0.79	0.94
R_{shunt} (Ω.cm^2)	62.29	3229.32	49.64	2367.3	198.57	486.49
R_{series} (Ω.cm^2)	9.03	7.82	15.75	5.89	35.83	7.98

Figure 7. Shelf-life statistical distribution of PCE values and *J*–*V* curves of champion devices of CZDTF (a, b) and CZDBT (c, d) under 1 sun illumination.

HTL-based devices. However, these devices, measured after 36 days, already showed a large spread in photovoltaic performance compared to the fresh devices. After 120 days, again the yield of the working devices was poor with PCE mostly around 1%.

■ CONCLUSIONS

The derivatives of disubstituted dibenzothiophene and spiro[1,3-dithiolane-2,9′-fluorene] were synthesized exploiting microwave irradiation-assisted Buchwald–Hartwig cross-coupling reactions. Stability, conductivity, hole-transporting, and hole-injecting properties of the synthesized compounds were examined before the development of perovskite solar cells. According to the Poole–Frenkel predictions of dependencies of charge mobility on the electric field, the derivatives of dibenzothiophene and spiro[1,3-dithiolane-2,9′-fluorene] can reach hole mobilities of 1×10^{-3} and 3×10^{-3} cm^2/V·s, respectively, at an electric field of 1×10^6 V/cm. The spiro[1,3-dithiolane-2,9′-fluorene] derivative demonstrates high conductivity according to the charge carrier extraction by linearly increasing voltage

https://doi.org/10.1021/acsaem.6c01031
ACS Appl. Energy Mater. XXXX, XXX, XXX–XXX

experiments. The high morphological stability of the solid amorphous films of this compound can be expected, due to its high glass transition temperature of 163 °C. A better combination of properties and characteristics of the derivatives of spiro[1,3-dithiolane-2,9′-fluorene], compared to those of the dibenzothiophene derivative, results in better output parameters of the developed perovskite solar cells under solar and indoor illumination. Maximum power conversion efficiencies of 15.5% under solar illumination and 30% under indoor illumination were achieved, demonstrating better performance of spiro[1,3-dithiolane-2,9′-fluorene] derivatives compared to dibenzothiophene derivatives. These findings should be useful for the molecular design of new stable and efficient hole-transporting materials for perovskite solar cells.

■ ASSOCIATED CONTENT

Supporting Information

The Supporting Information is available free of charge at https://pubs.acs.org/doi/10.1021/acsaem.6c01031.

Additional information on the experiments, materials and synthesis, computational calculations, fabrication and testing of PSCs, thermal characteristics, photophysical properties, charge-transporting data, output parameters of PSCs, and effect of thermal annealing on output parameters of PSCs (DOCX)

■ AUTHOR INFORMATION

Corresponding Authors

Lethy Krishnan Jagadamma – *Energy Harvesting Research Group, School of Physics and Astronomy, SUPA, University of St Andrews, St Andrews KY16 9SS, Scotland, U.K.;* orcid.org/0000-0002-4339-2484; Email: lkj2@st-andrews.ac.uk

Juozas Vidas Grazulevicius – *Department of Polymer Chemistry and Technology, Kaunas University of Technology, Baršausko Str. 59, LT-51423 Kaunas, Lithuania;* orcid.org/0000-0002-4408-9727; Email: juozas.grazulevicius@ktu.lt

Authors

Nagharsh Mirakyan – *Department of Polymer Chemistry and Technology, Kaunas University of Technology, Baršausko Str. 59, LT-51423 Kaunas, Lithuania; Scientific Technological Center of Organic and Pharmaceutical Chemistry of NAS RA, 26 Azatutyan Str., Yerevan 0014, Armenia*

Adnan Ahmed – *Department of Polymer Chemistry and Technology, Kaunas University of Technology, Baršausko Str. 59, LT-51423 Kaunas, Lithuania*

Asta Dabuliene – *Department of Polymer Chemistry and Technology, Kaunas University of Technology, Baršausko Str. 59, LT-51423 Kaunas, Lithuania*

Edwin Pineda – *Energy Harvesting Research Group, School of Physics and Astronomy, SUPA, University of St Andrews, St Andrews KY16 9SS, Scotland, U.K.*

Ranush Durgaryan – *Department of Chemistry—Ångström Laboratory, Physical Chemistry, Uppsala University, Ångströmlaboratoriet, Lägerhyddsvägen 1, 751 20 Uppsala, Sweden*

Dmytro Volyniuk – *Department of Polymer Chemistry and Technology, Kaunas University of Technology, Baršausko Str. 59, LT-51423 Kaunas, Lithuania;* orcid.org/0000-0003-3526-2679

Oleksandr Bezvikonnyi – *Department of Polymer Chemistry and Technology, Kaunas University of Technology, Baršausko Str. 59, LT-51423 Kaunas, Lithuania; Institute of Solid State Physics, University of Latvia, Kengaraga 8, LV-1063 Riga, Latvia*

Graeme Cooke – *School of Chemistry, University of Glasgow, Joseph Black Building, Glasgow G12 8QQ, Scotland, U.K.;* orcid.org/0000-0003-0890-5720

Complete contact information is available at: https://pubs.acs.org/doi/10.1021/acsaem.6c01031

Notes

The authors declare no competing financial interest.

■ ACKNOWLEDGMENTS

This project has received funding from the Research Council of Lithuania (LMTLT), agreement No. S-MIP-24-6. L.K.J. acknowledges funding from UKRI-FLF through MR/T022094/1.

■ REFERENCES

(1) Yang, C.; Hu, W.; Liu, J.; Han, C.; Gao, Q.; Mei, A.; Zhou, Y.; Guo, F.; Han, H. Achievements, Challenges, and Future Prospects for Industrialization of Perovskite Solar Cells. *Light: Sci. Appl.* **2024**, *13*, 227.

(2) Seyisi, T.; Fouda-Mbanga, B. G.; Mnyango, J. I.; Nthwane, Y. B.; Nyoni, B.; Mhlanga, S.; Hlangothi, S. P.; Tywabi-Ngeva, Z. Major Challenges for Commercialization of Perovskite Solar Cells: A Critical Review. *Energy Rep.* **2025**, *13*, 1400.

(3) Chen, Z.; Zhang, S.; Zhang, T.; Dai, J.; Yu, Y.; Li, H.; Hao, X.; Hou, J. Simplified Fabrication of High-Performance Organic Solar Cells through the Design of Self-Assembling Hole-Transport Molecules. *Joule* **2024**, *8* (6), 1723.

(4) Zhang, X.; Wu, S.; Zhang, H.; Jen, A. K. Y.; Zhan, Y.; Chu, J. Advances in Inverted Perovskite Solar Cells. *Nat. Photonics* **2024**, *18*, 1243.

(5) Li, S.; Cao, Y. L.; Li, W. H.; Bo, Z. S. A Brief Review of Hole Transporting Materials Commonly Used in Perovskite Solar Cells. *Rare Met.* **2021**, *40*, 2712.

(6) Murugan, P.; Hu, T.; Hu, X.; Chen, Y. Advancements in Organic Small Molecule Holetransporting Materials for Perovskite Solar Cells: Past and Future. *J. Mater. Chem. A* **2022**, *10*, 5044.

(7) Urieta-Mora, J.; García-Benito, I.; Molina-Ontoria, A.; Martín, N. Hole Transporting Materials for Perovskite Solar Cells: A Chemical Approach. *Chem. Soc. Rev.* **2018**, *47*, 8541.

(8) Yan, W.; Ye, S.; Li, Y.; Sun, W.; Rao, H.; Liu, Z.; Bian, Z.; Huang, C. Hole-Transporting Materials in Inverted Planar Perovskite Solar Cells. *Adv. Energy Mater.* **2016**, *6*, 1600474.

(9) Rezaee, E.; Liu, X.; Hu, Q.; Dong, L.; Chen, Q.; Pan, J. H.; Xu, Z. X. Dopant-Free Hole Transporting Materials for Perovskite Solar Cells. *Sol. RRL* **2018**, *2* (11), 1800200.

(10) Tumen-Ulzii, G.; Matsushima, T.; Adachi, C. Mini-Review on Efficiency and Stability of Perovskite Solar Cells with Spiro-OMeTAD Hole Transport Layer: Recent Progress and Perspectives. *Energy Fuels* **2021**, *35*, 18915.

(11) Yuan, J.; Zhang, Y.; Zhou, L.; Zhang, G.; Yip, H. L.; Lau, T. K.; Lu, X.; Zhu, C.; Peng, H.; Johnson, P. A.; Leclerc, M.; Cao, Y.; Ulanski, J.; Li, Y.; Zou, Y. Single-Junction Organic Solar Cell with over 15% Efficiency Using Fused-Ring Acceptor with Electron-Deficient Core. *Joule* **2019**, *3* (4), 1140.

(12) Saliba, M.; Orlandi, S.; Matsui, T.; Aghazada, S.; Cavazzini, M.; Correa-Baena, J. P.; Gao, P.; Scopelliti, R.; Mosconi, E.; Dahmen, K.

H.; De Angelis, F.; Abate, A.; Hagfeldt, A.; Pozzi, G.; Graetzel, M.; Nazeeruddin, M. K. A Molecularly Engineered Hole-Transporting Material for Efficient Perovskite Solar Cells. *Nat. Energy* **2016**, *1* (2), 15017.

(13) Wang, S.; Edwards, P. R.; Abdelsamie, M.; Brown, P.; Webster, D.; Ruseckas, A.; Rajan, G.; Neves, A. I. S.; Martin, R. W.; Sutter-Fella, C. M.; Turnbull, G. A.; Samuel, I. D. W.; Jagadamma, L. K. Chlorine Retention Enables the Indoor Light Harvesting of Triple Halide Wide Bandgap Perovskites. *J. Mater. Chem. A* **2023**, *11* (23), 12328–12341.

(14) Wang, S.; Kang, B. C.; Park, S. J.; Ha, T. J.; Krishnan Jagadamma, L. P3HT vs Spiro-OMeTAD as a Hole Transport Layer for Halide Perovskite Indoor Photovoltaics and Self-Powering of Motion Sensors. *J. Phys. Mater.* **2023**, *6* (2), 024004.

(15) Mesquita, I.; Andrade, L.; Mendes, A. Temperature Impact on Perovskite Solar Cells Under Operation. *ChemSusChem* **2019**, *12* (10), 2186.

(16) Shaka, A. W.; Wang, S.; Maria Joseph Raj, N. P.; Muddam, R. S.; McKeown, N. B.; Taylor, D.; Krishnan Jagadamma, L.; Cooke, G. Spirobisindane-Based Hole Transporting Materials for Conventional and Indoor Halide Perovskite Solar Cells. *Sol. RRL* **2025**, *9* (16), 2500208.

(17) Bach, U.; Lupo, D.; Comte, P.; Moser, J. E.; Weissörtel, F.; Salbeck, J.; Spreitzer, H.; Grätzel, M. Solid-State Dye-Sensitized Mesoporous TiO_2 Solar Cells with High Photon-to-Electron Conversion Efficiencies. *Nature* **1998**, *395*, 583.

(18) Rombach, F. M.; Haque, S. A.; Macdonald, T. J. Lessons Learned from Spiro-OMeTAD and PTAA in Perovskite Solar Cells. *Energy Environ. Sci.* **2021**, *14*, 5161.

(19) Schloemer, T. H.; Christians, J. A.; Luther, J. M.; Sellinger, A. Doping Strategies for Small Molecule Organic Hole-Transport Materials: Impacts on Perovskite Solar Cell Performance and Stability. *Chem. Sci.* **2019**, *10* (7), 1904.

(20) Ye, L.; Wu, J.; Catalán-Gómez, S.; Yuan, L.; Sun, R.; Chen, R.; Liu, Z.; Ulloa, J. M.; Hierro, A.; Guo, P.; Zhou, Y.; Wang, H. Superoxide Radical Derived Metal-Free Spiro-OMeTAD for Highly Stable Perovskite Solar Cells. *Nat. Commun.* **2024**, *15* (1), 7889.

(21) Ma, F.; Zhao, Y.; Qu, Z.; Yu, S.; Chu, Z.; Xiong, Z.; Zhou, J.; Wei, Z.; Zhang, X.; You, J. Efficient Perovskite Solar Cells with Iodine-Doped Spiro-OMeTAD Hole Transport Layer via Fast Oxidation. *Sol. RRL* **2023**, *7* (10) 2300042.

(22) Jiang, B. H.; Gao, Z. J.; Lung, C. Y.; Shi, Z. E.; Du, H. Y.; Su, Y. W.; Shih, H. S.; Lee, K. M.; Hung, H. H.; Chan, C. K.; Chen, C. P.; Wong, K. T. Enhancing the Efficiency of Indoor Perovskite Solar Cells through Surface Defect Passivation with Coplanar Heteroacene Cored A–D–A-Type Molecules. *Adv. Funct. Mater.* **2024**, *34* (19), 2312819.

(23) Goje, A. A.; Ludin, N. A.; Fahsyar, P. N. A.; Syafiq, U.; Chelvanathan, P.; Syakirin, A. D. A. G.; Teridi, M. A.; Ibrahim, M. A.; Su'ait, M. S.; Sepeai, S.; Yasir, A. S. H. M. Review of Flexible Perovskite Solar Cells for Indoor and Outdoor Applications. *Mater. Renewable Sustainable Energy* **2024**, *13* (1), 155.

(24) Yang, Y.; Senanayake, S.; Hoang, M. T.; Ye, J.; Pham, N. D.; Wang, H. Non-Metallic Back Contacts for Indoor Perovskite Solar Cells: Material Criteria, Recent Progress, and Future Outlook. *Adv. Mater.* **2026**, *38*, e12402.

(25) Best Research-Cell Efficiency Chart | Photovoltaic Research | NREL, n.d. Https://Www.Nrel.Gov/Pv/Cell-Efficiency (accessed Nov 21, 2025).

(26) Li, S.; Jiang, Y.; Xu, J.; Wang, D.; Ding, Z.; Zhu, T.; Chen, B.; Yang, Y.; Wei, M.; Guo, R.; Hou, Y.; Chen, Y.; Sun, C.; Wei, K.; Qaid, S. M. H.; Lu, H.; Tan, H.; Di, D.; Chen, J.; Grätzel, M.; Sargent, E. H.; Yuan, M. High-Efficiency and Thermally Stable $FACsPbI_3$ Perovskite Photovoltaics. *Nature* **2024**, *635* (8037), 82.

(27) Dastgeer, G.; Nisar, S.; Zulfiqar, M. W.; Eom, J.; Imran, M.; Akbar, K. A Review on Recent Progress and Challenges in High-Efficiency Perovskite Solar Cells. *Nano Energy* **2024**, *132*, 110401.

(28) Luo, X.; Boschloo, G.; Kloo, L.; Sun, L.; Xu, B. Spiro[Fluorene-9,9′-Xanthene]-Based Hole-Transporting Materials for Photovoltaics: Molecular Design, Structure-Property Relationship, and Applications. *Acc. Mater. Res.* **2024**, *5* (2), 220–235.

(29) Xu, B.; Zhang, J.; Hua, Y.; Liu, P.; Wang, L.; Ruan, C.; Li, Y.; Boschloo, G.; Johansson, E. M. J.; Kloo, L.; Hagfeldt, A.; Jen, A. K. Y.; Sun, L. Tailor-Making Low-Cost Spiro[Fluorene-9,9′-Xanthene]-Based 3D Oligomers for Perovskite Solar Cells. *Chem* **2017**, *2* (5), 676.

(30) Sallenave, X.; Shasti, M.; Anaraki, E. H.; Volyniuk, D.; Grazulevicius, J. V.; Zakeeruddin, S. M.; Mortezaali, A.; Grätzel, M.; Hagfeldt, A.; Sini, G. Interfacial and Bulk Properties of Hole Transporting Materials in Perovskite Solar Cells: Spiro-MeTADversusspiro-OMeTAD. *J. Mater. Chem. A* **2020**, *8* (17), 8527–8539.

(31) Tingare, Y. S.; Liu, L. Y.; Su, C.; Lin, W. Z.; Yen, C. Y.; Chen, W. H.; Teng, S. H.; Chen, M. J.; Chu, C. W.; Li, W. R. Sulfur-Rich Hole-Transporting Materials for Inverted Perovskite Solar Cells. *Org. Lett.* **2025**, *27* (26), 6983.

(32) Zhang, A.; Chen, Y.; Xu, Y.; Wang, H.; Zong, X.; Sun, Z.; Liang, M.; Xue, S. Flexible Substituted Benzo[1,2-B:4,5-B']Dithiophene-Cored D-π-D Hole-Transporting Materials for Perovskite Solar Cells. *ACS Appl. Energy Mater.* **2024**, *7* (24), 11741.

(33) Venkateswarlu, S.; Lin, Y. D.; Lee, K. M.; Liau, K. L.; Tao, Y. T. Thiophene-Fused Butterfly-Shaped Polycyclic Arenes with a Diphenanthro[9,10- b:9′,10′- d]Thiophene Core for Highly Efficient and Stable Perovskite Solar Cells. *ACS Appl. Mater. Interfaces* **2020**, *12* (45), 50495.

(34) Liu, Y.; Zhan, X.; Leu, Y. High-Mobility Conjugated Polymers Based on Fused-Thiophene Building Blocks. *Macromol. Chem. Phys.* **2011**, *212* (5), 428-443.

(35) Zhou, J.; Chen, L.; Ma, Z.; Liao, X.; Yan, Y.; Chen, Z.; Yang, Y.; Wang, R.; Yu, W.; Wang, Y.; Nie, X.; Huo, P.; Fang, X.; Zhang, J.; Zhou, Y.; Song, B.; Yuan, N. Dibenzothiophene S, S-Dioxide-Containing Dipolar Molecules As Efficient Hole-Transport Materials for p-i-n Perovskite Solar Cells. *ACS Appl. Mater. Interfaces* **2024**, *16* (42), 57851–57859.

(36) Durgaryan, R.; Simokaitiene, J.; Volyniuk, D.; Bezvikonnyi, O.; Danyliv, Y.; Kim, B. J.; Woon, K. L.; Sini, G.; Boschloo, G.; Grazulevicius, J. V. Enhancement of Hole Extraction Efficiency of Dibenzothiophenes by Substitution Engineering: Toward Additive-Free Perovskite Solar Cells with Power Conversion Efficiency Exceeding 20%. *Sol. RRL* **2022**, *6* (7), 2200128.

(37) Rakstys, K.; Paek, S.; Drevilkauskaite, A.; Kanda, H.; Daskeviciute, S.; Shibayama, N.; Daskeviciene, M.; Gruodis, A.; Kamarauskas, E.; Jankauskas, V.; Getautis, V.; Nazeeruddin, M. K. Carbazole-Terminated Isomeric Hole-Transporting Materials for Perovskite Solar Cells. *ACS Appl. Mater. Interfaces* **2020**, *12* (17), 19710.

(38) Jeong, M.; Choi, I. W.; Yim, K.; Jeong, S.; Kim, M.; Choi, S. J.; Cho, Y.; An, J. H.; Kim, H. B.; Jo, Y.; Kang, S. H.; Bae, J. H.; Lee, C. W.; Kim, D. S.; Yang, C. Large-Area Perovskite Solar Cells Employing Spiro-Naph Hole Transport Material. *Nat. Photonics* **2022**, *16* (2), 119–125.

(39) Han, M.; Liang, Y.; Chen, J.; Zhang, X.; Ghadari, R.; Liu, X.; Wu, N.; Wang, Y.; Zhou, Y.; Ding, Y.; Cai, M.; Chen, H.; Dai, S. A N-Ethylcarbazole-Terminated Spiro-Type Hole-Transporting Material for Efficient and Stable Perovskite Solar Cells. *ChemSusChem* **2022**, *15* (20), e202201485.

(40) Zhou, J.; Tan, L.; Liu, Y.; Li, H.; Liu, X.; Li, M.; Wang, S.; Zhang, Y.; Jiang, C.; Hua, R.; Tress, W.; Meloni, S.; Yi, C. Highly Efficient and Stable Perovskite Solar Cells via a Multifunctional Hole Transporting Material. *Joule* **2024**, *8* (6), 1691.

(41) Liu, X.; Zhang, X.; Zhou, Y.; Dai, W.; Chen, J.; Syzgantseva, O. A.; Syzgantseva, M. A.; Li, B.; Ghadari, R.; Han, M.; Du, W.; Shao, Z.; Wang, Q.; Dai, S.; Nazeeruddin, M. K.; Ding, Y. Efficient and Stable Perovskite Solar Cells with a Multifunctional Spiro-Based Hole Transport Material. *Adv. Funct. Mater.* **2025**, *35* (6), 2415179.

(42) Wang, S.; Kodalle, T.; Millar, S.; Sutter-Fella, C. M.; Krishnan Jagadamma, L. Metal Oxide vs Organic Semiconductor Charge Extraction Layers for Halide Perovskite Indoor Photovoltaics. *Small Sci.* **2024**, *4* (12), 2400292.

(43) Tan, J. K.; Png, R. Q.; Zhao, C.; Ho, P. K. H. Ohmic Transition at Contacts Key to Maximizing Fill Factor and Performance of Organic Solar Cells. *Nat. Commun.* **2018**, *9* (1), 3269.
(44) Steim, R.; Ameri, T.; Schilinsky, P.; Waldauf, C.; Dennler, G.; Scharber, M.; Brabec, C. J. Organic Photovoltaics for Low Light Applications. *Sol. Energy Mater. Sol. Cells* **2011**, *95* (12), 3256.
(45) Shi, Z. E.; Cheng, T. H.; Lung, C. Y.; Lin, C. W.; Wang, C. L.; Jiang, B. H.; Hsiao, Y. S.; Chen, C. P. Achieving over 42 % Indoor Efficiency in Wide-Bandgap Perovskite Solar Cells through Optimized Interfacial Passivation and Carrier Transport. *Chem. Eng. J.* **2024**, *498*, 155512.
(46) Yuan, Y.; Li, H.; Luo, H.; Zhang, Y.; Li, X.; Jiang, T.; Yang, Y.; Liu, L.; Fan, B.; Hao, X. A Comprehensive Review of Self-Assembled Monolayers as Hole-Transport Layers in Inverted Perovskite Solar Cells. *Energies* **2025**, *18* (10), 2577.
(47) Wang, S.; Guo, H.; Wu, Y. Advantages and Challenges of Self-Assembled Monolayer as a Hole-Selective Contact for Perovskite Solar Cells. *Mater. Futures* **2023**, *2*, 012105.
(48) Khambunkoed, N.; Chen, F. C. Perovskite Indoor Photovoltaic Devices for Internet of Things Applications. *J. Phys.: Energy* **2025**, *7*, 032003.
(49) Cevher, S. C.; Pernstich, K. P. Novel Integrated Reference-Counter Electrode for Electrochemical Measurements of HOMO and LUMO Levels in Small-Molecule Thin-Film Semiconductors for OLEDs. *Org. Electron.* **2025**, *136*, 107152.
(50) Nakka, L.; Cheng, Y.; Aberle, A. G.; Lin, F. Analytical Review of Spiro-OMeTAD Hole Transport Materials: Paths Toward Stable and Efficient Perovskite Solar Cells. *Adv. Energy Sustainability Res.* **2022**, *3*, 2200045.
(51) Shao, S.; Loi, M. A. The Role of the Interfaces in Perovskite Solar Cells. *Adv. Mater. Interfaces* **2020**, *7*, 1901469.
(52) Du, T.; Qiu, S.; Zhou, X.; Corre, V. M., Le; Wu, M.; Dong, L.; Peng, Z.; Zhao, Y.; Jang, D.; Spiecker, E.; Brabec, C. J.; Egelhaaf, H. J. Efficient, Stable, and Fully Printed Carbon-Electrode Perovskite Solar Cells Enabled by Hole-Transporting Bilayers. *Joule* **2023**, *7* (8), 1920.
(53) Umezawa, Y. Letters to the Editor the 52nd Symposium on Analytical Chemistry. *Anal. Sci.* **1991**, *7*, 525.
(54) Kočka, J.; Arlauskas, K.; Viliūnas, M. Extraction Current Transients: New Method of Study of Charge Transport in Microcrystalline Silicon. *Phys. Rev. Lett.* **2000**, *84* (21), 4946–4949.
(55) Stephen, M.; Genevičius, K.; Juška, G.; Arlauskas, K.; Hiorns, R. C. Charge Transport and Its Characterization Using Photo-CELIV in Bulk Heterojunction Solar Cells. *Polym. Int.* **2017**, *66*, 13.
(56) Mallo, N.; McAnally, S.; Jin, H.; Brooks, E.; Chu, R.; Babazadeh, M.; Smyth, J.; Huang, D. M.; Hight-Huf, N.; Reid, O. G.; Rumbles, G.; Burn, P. L.; Gentle, I. R.; Shaw, P. E. Free-Charge Carrier Generation in Homojunction Non-Polymeric Organic Semiconductor Films – The Role of the Optical Frequency Dielectric Constant. *Adv. Opt. Mater.* **2024**, *12* (36), 2401825.
(57) Neukom, M. T.; Züfle, S.; Ruhstaller, B. Reliable Extraction of Organic Solar Cell Parameters by Combining Steady-State and Transient Techniques. *Org. Electron.* **2012**, *13* (12), 2910.
(58) Karasyuk, P.; Shepelytskyi, Y.; Semeniuk, O.; Bubon, O.; Juska, G.; Blevis, I.; Reznik, A. Investigation of Photoconductivity and Electric Field Distribution in CZT Detectors by Time-of-Flight (TOF) and Charge Extraction by Linearly Increasing Voltage (CELIV). *J. Mater. Sci.: Mater. Electron.* **2018**, *29* (16), 13941.
(59) Armin, A.; Juska, G.; Philippa, B. W.; Burn, P. L.; Meredith, P.; White, R. D.; Pivrikas, A. Doping-Induced Screening of the Built-in-Field in Organic Solar Cells: Effect on Charge Transport and Recombination. *Adv. Energy Mater.* **2013**, *3* (3), 321–327.
(60) Grynko, O.; Juška, G.; Reznik, A. Charge Extraction by Linearly Increasing Voltage (CELIV) Method for Investigation of Charge Carrier Transport and Recombination in Disordered Materials. *Photoconductivity and Photoconductive Materials: Fundamentals, Techniques and Applications: Volume 1 and 2*; John Wiley & Sons, Inc., **2022**; Vol. *1–2*.
(61) Pivrikas, A.; Sariciftci, N. S.; Juška, G.; Österbacka, R. A Review of Charge Transport and Recombination in Polymer/Fullerene Organic Solar Cells. *Prog. Photovoltaics Res. Appl.* **2007**, *15* (8), 677–696.
(62) Toikkonen, S.; Grandhi, G. K.; Wang, S.; Baydin, B.; Al-Anesi, B.; Jagadamma, L. K.; Vivo, P. Is Doping of Spiro-OMeTAD a Requirement for Efficient and Stable Perovskite Indoor Photovoltaics? *Adv. Devices Instrum.* **2024**, *5*, 0048.
(63) Orwat, B.; Shi, Z. E.; Ma, C. H.; Jankowska, K.; Nawrocik, J.; Singh, A.; Zheng, Y. H.; Tu, W. C.; Ling, Z.; Dąbczyński, P.; Rogala, M.; Krukowski, P.; Kowalczyk, P. J.; Data, P.; Łuszczyńska, B.; Kownacki, I.; Chen, C. P. Highly Efficient Indoor Perovskite Solar Cells with 40% Efficiency Using Perylene Diimide-Based Zwitterionic Cathode Interlayers. *Small* **2025**, *21* (17), 2411623.
(64) Xie, G.; Chen, L.; Liu, J.; Yu, J.; Yin, H.; Li, H.; Yang, Y.; Liang, A.; Chen, Y. Recent Progress in Spiro-Type Hole Transport Materials for Efficient and Stable Perovskite Solar Cells. *J. Mater. Chem. C* **2024**, *13*, 2040.

https://doi.org/10.1021/acsaem.6c01031
ACS Appl. Energy Mater. XXXX, XXX, XXX–XXX